Numerical simulation of air distribution in a room with a sidewall jet under benchmark test conditions

Cite as: AIP Conference Proceedings **1959**, 050033 (2018); https://doi.org/10.1063/1.5034661
Published Online: 02 May 2018

Marina Zasimova, and Nikolay Ivanov

Numerical Simulation of Air Distribution in a Room with a Sidewall Jet under Benchmark Test Conditions

Marina Zasimova [a)] and Nikolay Ivanov [b)]

Department of Fluid Dynamics, Combustion and Heat Transfer, Peter the Great St.Petersburg Polytechnic University, 29 Polytechnicheskaya str., St.Petersburg, 195251, Russia

[a)]Corresponding author: zasimova_ma@spbstu.ru
[b)]ivanov_ng@spbstu.ru

Abstract. The goal of the study is to validate Large Eddy Simulation (LES) data on mixing ventilation in an isothermal room at conditions of benchmark experiments by Hurnik et al. (2015). The focus is on the accuracy of the mean and rms velocity fields prediction in the quasi-free jet zone of the room with 3D jet supplied from a sidewall rectangular diffuser. Calculations were carried out using the ANSYS Fluent 16.2 software with an algebraic wall-modeled LES subgrid-scale model. CFD results on the mean velocity vector are compared with the Laser Doppler Anemometry data. The difference between the mean velocity vector and the mean air speed in the jet zone, both LES-computed, is presented and discussed.

INTRODUCTION

To provide comfortable and safety conditions for occupants, HVAC (heating, ventilation and air conditioning) systems should control and maintain key indoor environmental parameters within required limits. Design of efficient HVAC systems able to do so requires for detailed air distribution analysis. Computational Fluid Dynamics (CFD) modeling of airflow in ventilated indoor spaces allows predicting 3D velocity, temperature and contaminant concentration distributions and is nowadays widely involved into the design practice. CFD modeling based on the Reynolds-Averaged Navier-Stokes (RANS) equations solution is widely used in various industrial applications related to HVAC system design. Examples could be given from transportation, e.g. development of personalized ventilation in commercial airplanes [1] and evaluation of a truck cabin ventilation [2], and from construction, e.g. design of ventilation systems for an indoor arena [3] or a historic auditorium [4]. As well, there are examples of CFD application to evaluation of the ECLSS (environmental control and life support systems) operation, like carbon dioxide [5] or ammonia [6] concentration control on board of the International Space Station. Less empirical than RANS, vortex-resolving Large Eddy Simulation (LES) approach is still not widely used in the engineering practice, but it is expected to be a helpful tool in the nearest future [7].

Both RANS and LES results demand comprehensive validation, as there are many sources of uncertainties in CFD data, mostly due to turbulence modeling. To validate CFD results, well-documented benchmark experimental data obtained in simplified room configurations are required. Extended description of most representative mixing ventilation benchmark experiments with the correspondent reference list is given in [8]. The most popular isothermal benchmark test is the 2D test by Nielsen et al. [9]. The test data on mean velocity and fluctuations measured with the Laser-Doppler Anemometry (LDA) are available in [9] and on the website http://www.cfd-benchmarks.com/. These data have been used in more than 50 papers for CFD validation during the last two decades. An example of isothermal ventilation test flow for more complicated geometry is the configuration considered by Posner et al. [10] where LDA and particle image velocimetry (PIV) measurements were performed in a room with a large flow obstruction.

Several tests deal with a single 3D jet supplied from a diffuser to the confined space. In mixing ventilation systems diffusers are often located at side walls, above the inhabitants, and it is necessary to predict correctly not only the jet behavior, but also interaction between the jet, characterized by high velocities, and the low-velocity zone of induced secondary flows (occupied zone). Recent experiments by Hurnik et al. [8, 11] are the only example of a 3D test for a

The Eighth Polyakhov's Reading
AIP Conf. Proc. 1959, 050033-1–050033-8; https://doi.org/10.1063/1.5034661
Published by AIP Publishing. 978-0-7354-1660-4/$30.00

room with a sidewall jet with pronounced division into the jet and occupied zones. 3D jet supplied from a rectangular sidewall diffuser was studied using the LDA measurements (two air velocity components were measured with the uncertainty lower than 5%), while velocity fields in the occupied zone were measured with the omnidirectional low velocity thermal anemometers (LVTA) techniques. The full data set on velocity measurement results is provided in a special file attached to [11]. In the present study, LES modeling of the airflow at conditions of benchmark test by Hurnik et al. is performed and velocity fields in the jet zone are discussed in comparison with the experimental data.

PROBLEM FORMULATION

Test Room Geometry and Boundary Conditions

Figure 1a illustrates the computational domain adopted for indoor ventilation problem corresponding to the test facility [8]. The origin of the coordinate system is in the corner of the room. The room dimensions are $H = 3$ m, $L = 6$ m, $W = 6$ m. Rectangular inlet of $b = 0.144$ m, $h = 0.096$ m (equivalent diameter $D_e = 0.133$ m) is located on the sidewall; its center is positioned at the distance of $H_{in} = 2.35$ m from the floor, at the mid-line with respect to transversal direction (see Fig. 1b). The outlet located at the same sidewall just above the floor has the same dimensions as the inlet. Note that although the measurements were performed in the 1:5 physical model, all the experimental results presented in [8] were recalculated to the prototype conditions.

The LDA measurement data on the longitudinal (x) and transversal (z) components of velocity in the quasi-free jet zone are available at eighteen lines shown in Fig. 1a (at two perpendicular measurement planes). The measurement planes crossed at the middle of the supply openings; x-coordinates of the measurement lines are given in Table 1.

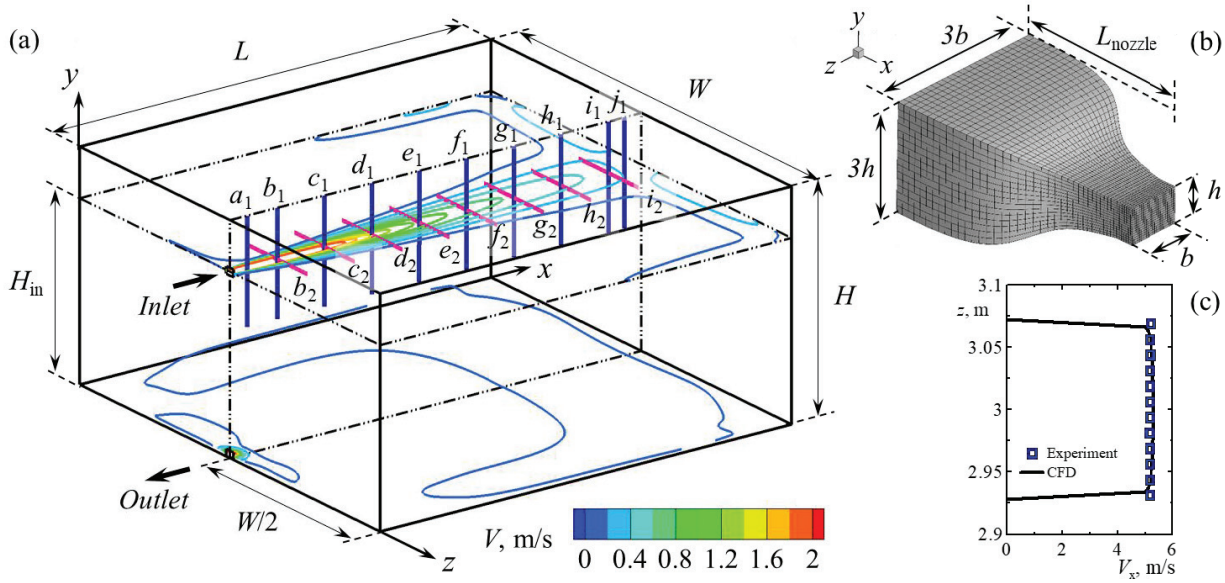

FIGURE 1. (a) Computational domain; the plot shows measurement lines positions and isolines of mean velocity magnitude at sections $y = 2.35$ m, $y = 0.048$ m; (b) inlet nozzle used for inflow simulation; (c) inlet velocity profile at $y = 2.35$ m

TABLE 1. The x-coordinate values of vertical and horizontal lines with the measurement data

a_1	b_1, b_2	c_1, c_2	d_1, d_2	e_1, e_2	f_1, f_2	g_1, g_2	h_1, h_2	i_1, i_2	j_1
0.25	0.69	1.38	2.07	2.76	3.45	4.14	4.83	5.52	5.75

Air was assumed as an incompressible fluid with constant physical properties ($\rho = 1.2$ kg/m^3, $\mu = 1.8\times10^{-5}$ kg/m·s). According to the experimental conditions for the full-scale prototype, the bulk velocity at the inlet slot was $U_{bulk} = 5.16$ m/s that corresponded to the Reynolds number $Re = \rho D_e U_{bulk}/\mu = 4.57\times10^4$ (as mentioned in [8], $Re_{exp} = 4.53\times10^4$; note that five times higher velocity was set in the model experiments to keep the same Re). In order

to set the inlet velocity profile, turbulent airflow in the nozzle with rectangular cross-section shown in Fig. 1b was computed. The length of the nozzle was L_{nozzle} = 0.6 m, the contraction ratio was equal to three (less than in [8]). This auxiliary problem was solved using RANS approach based on the standard k-ε turbulence model; the grid of about 100,000 cells was used (Fig. 1b). The computed profile corresponds to the experimental data (see Fig. 1c); the measured inlet flow rate and mean velocity are completely reproduced in the CFD boundary conditions.

Computational Grid

The computational grids created with the ANSYS ICEM CFD 16.2 mesh generator consisted of hexahedral mesh elements clustered to the walls and to the inlet and outlet sections. The height of the first near-wall cell was 0.005 m at x = 0 wall (with the supply diffuser) and at y-walls. It was two times higher, 0.01 m, at x = 6 m wall and z-walls. The basic grid contained 216×242×304 elements that corresponded to about 16 million cells. Figure 2a gives a distribution of the normalized distance from the center of the first computational cell to the wall, y^+. The distribution represents not only the flow pattern peculiarities discussed below, but also the variation in the height of the first near-wall cells. The peak y^+ values are about 30 in the zone of the jet impingement (at the sidewall x = 6 m opposite to the inlet opening); y^+ values are mostly in the range from 5 to 10 at z-walls and less than five at y-walls.

The grid dimension choice was based on the mesh-sensitivity analysis of LES solutions performed previously for the Nielsen et al. test problem at lower Re values [12]. For the current test by Hurnik et al., initial results of the computations with the refined grid of about 35 million cells (278×350×355) did not demonstrate any changes in the time-averaged solution. It is possible to conclude that mesh dependence of the LES results presented is negligible.

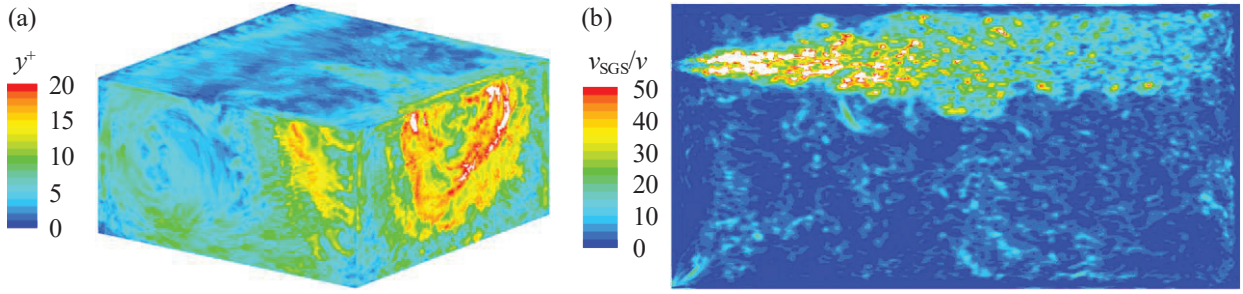

FIGURE 2. (a) An instantaneous distribution of the normalized distance from the first computational cell to the wall; (b) instantaneous SGS to molecular viscosity ratio at the vertical mid-section z = 3 m

Turbulence Modeling

Turbulent airflow in the room was computed using the LES approach that solves the filtered Navier-Stokes equations resolving large scales of motion, while small scales are modeled with an appropriate subgrid-scale (SGS) model. The overview and outlook of LES could be found in [7].

For the incompressible fluid, the equations are written as follows:

$$\begin{cases} \nabla \cdot \vec{V} = 0 \\ \dfrac{\partial \vec{V}}{\partial t} + \nabla \cdot (\vec{V}\vec{V}) = -\dfrac{1}{\rho}\nabla \cdot p + 2\nu(\nabla \cdot \underline{S}) - \nabla \cdot \underline{\tau}^{SGS} \end{cases} \tag{1}$$

where V is the velocity vector with components (V_x, V_y, V_z), $\underline{S}$ is the strain rate tensor for the resolved motion, and $\underline{\tau}^{SGS}$ is the SGS stress term arising from the spatial filtering procedure. The filtering operation [7] for a variable f determines the filtered (resolved) and small-scale (non-resolved) components $\tilde{f}$ and f' as follows:

$$\tilde{f}(x,t) = \int_{Vol} G(x-x',\Delta) f(x',t) dx'^3 , \quad f' = f - \tilde{f}, \tag{2}$$

where $G(x - x', \Delta)$ is a filter function that determines the size and structure of the small scales, x is a coordinate of the point under consideration, and Δ is the filter width.

To determine the SGS stress term, the generalized Boussinesq hypothesis is used:

$$\tau_{ij}^{SGS} - \frac{1}{3}\tau_{kk}\delta_{ij} = -2\nu_{SGS}S_{ij}, \tag{3}$$

where ν_{SGS} is the SGS viscosity, which must be determined by a SGS model.

The algebraic Wall-Modeled LES (WMLES) S-Omega SGS model available in ANSYS Fluent was applied in the current study. The model realization in the code is based on [13], and the SGS viscosity is calculated with the use of a hybrid length scale and the wall-damping function:

$$\nu_{SGS} = min\left\{(\kappa d_w)^2, (C_S\Delta)^2\right\} \mid S-\Omega \mid \left(1-exp\left\{\left(-y^+/25\right)^3\right\}\right), \quad (4)$$

where S and Ω are the strain rate and vorticity magnitude, $C_S = 0.2$ is the Smagorinsky constant, $\kappa = 0.41$ is the von Karman constant, d_w is the distance to the nearest wall, y^+ is the normal to the wall inner scaling. The grid scale is defined as follows:

$$\Delta = min\left\{max\left(C_w d_w, C_w\Delta_{max}, \Delta_{wn}\right), \Delta_{max}\right\}, \quad (5)$$

where Δ_{max} and Δ_{wn} are the maximum local grid spacing and the grid step in the wall-normal direction, and $C_w = 0.15$ is the empirical constant.

To specify the time-evolving inflow conditions with superimposed perturbations on inlet mean velocity profiles, the vortex method available in ANSYS Fluent was used.

Figure 2b gives information on the non-resolved scales for the mesh used: the ratio of the SGS to molecular viscosity is in the range from 30 to 50 in the jet zone (and even higher in the mixing layers), and it is less than five in the occupied zone.

Solver Settings

Numerical solution was obtained with the CFD package ANSYS Fluent 16.2 based on the finite volume method with the cell-centered variable arrangement. The non-iterative time advancement scheme (NITA) based on the fractional step method was used. The spatial discretization was performed with the central-differencing scheme for convective terms, the second order pressure interpolation was used.

The second order implicit time integration was used. The value of a time step, Δt, is equal to 6×10^{-4} s, and it was chosen to provide the Courant number in the computational domain less than 1. To accumulate representative statistics, it was required to calculate samples of about 1.7 million time steps (1000 s). It was verified that the averaging time has been sufficient to obtain statistically steady data by monitoring the evolution of the mean velocity at several points.

All computations were carried out using the resources of the Peter the Great St.Petersburg Polytechnic University supercomputer center (scc.spbstu.ru). The computational resources used included 11 nodes of the Polytechnic RSC Tornado cluster. Each node has two CPUs Intel(R) Xeon(R) E5-2697v3 at 2.60 GHz, 14 cores each CPU; 308 cores were used in total for the parallel computations.

RESULTS AND DISCUSSION

Air Velocity Distributions

Velocity isolines shown in Fig. 1a illustrate the global airflow pattern in the room with a sidewall jet. Figure 3a gives more information on the flow structure: an instantaneous 3D isosurface of Q-criterion, $Q = 0.5(\Omega^2 - S^2)$, colored by velocity magnitude is given in the plot for a half of the room. In accordance with the experimental observations [8], it is visible that the jet formed at the rectangular inlet behaves as a free circular jet, moving straight onto the opposite sidewall. After interaction with the wall in the impingement region, air spreads along the sidewall and returns back towards the outlet forming the secondary recirculation airflow with relatively low velocities. The return flow is more intensive on the periphery, near the z-walls, while in the mid part of the room, below the jet, the return flow is weak. Skin friction distributions shown indirectly in Fig. 2a also illustrate secondary recirculation flow formation along the z-walls. LES data clearly indicate two airflow zones discussed in [8]: the jet zone and the occupied zone. These zones are visible very well in the distribution of the time-averaged velocity magnitude, $\langle V \rangle$, shown in Fig. 3b, from here and after $\langle\ \rangle$ denotes time averaging. Velocities in the occupied zone are less than 0.5 m/s (blue color) everywhere, except the small spherical region near the outlet section where velocities increase rapidly from the values lower than 0.3 m/s at the distance of about $3h$ from the outlet to the values higher than 5 m/s directly at the outlet. Irregular turbulent structures at the isosurface of $Q = 1.0$ s^{-2} are visible everywhere in the room (see Fig. 3a). The size of the vortex structures in the low-velocity occupied zone is larger than in the jet zone.

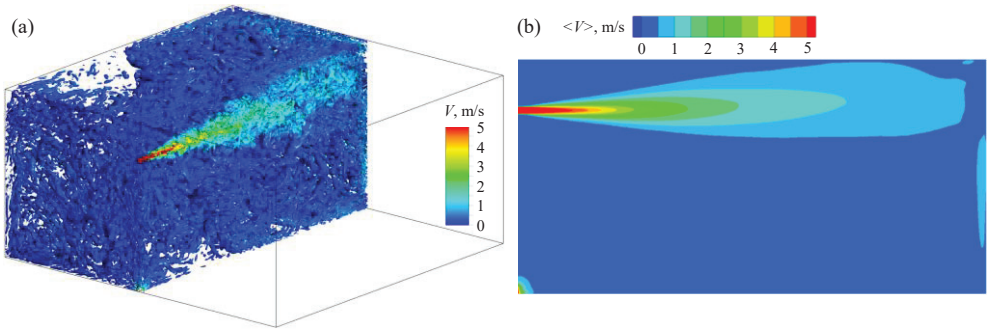

FIGURE 3. (a) Instantaneous isosurface of Q-criterion (Q = 1.0 s^{-2}) colored by velocity magnitude; (b) time-averaged velocity magnitude at mid-section z = 3 m

Comparison of LES Results with Experimental Data

Figures 4 and 5 directly compare computed and measured [8] profiles of mean longitudinal velocity, $<V_x>$, at two measurement planes. The plots give an evidence that the LES results reproduce accurately the jet evolution over the axial coordinate: the values and positions of the maximum velocity, as well as the width of the mixing shear layer in the jet zone obtained in the calculations and experiment are almost the same. Computational data reproduce well the recirculation zone formed in the corner of the room, under the ceiling (lines i_1 and j_1 in Fig. 4, at $y > 2.7$ m). The jet deflection towards the top wall obtained in the experiments is also reproduced, but with some delay, at higher values of axial coordinate: in experimental profiles this deflection is already visible at line f_1, while LES computations demonstrate an upward shift of the velocity maximum starting from line h_1 (see Fig. 4). Consequently, the difference between the computed and experimental data in the lower mixing layer is visible at lines f_1, g_1 and h_1, at y-coordinate in the range from 1.9 to 2.3 m.

Figure 5 demonstrates good agreement of computed and measured $<V_x>$-values at the horizontal measurement plane (y = 2.35 m). The symmetry of the velocity profile with respect to z-coordinate is reproduced completely. The only difference between the computed and experimental data is visible in the impingement zone: LES results demonstrate more pronounced deceleration at the last line i_2 than it is registered in the measurements.

The measured and computed rms pulsations of the longitudinal velocity, $<V_x'^2>^{0.5}$, at the vertical measurement plane (z = 3 m) are compared in Fig. 6. Good agreement is visible at lines from g_1, to j_1, i.e. far from the supply diffuser, at $x > 4.0$ m. At lines d_1 and f_1 that are at lower x-values, computations slightly underestimate pulsations in the jet core. Note that data at lines b_1, c_1 and e_1 are not shown to provide better plot layout; for these lines the difference between the LES and measured data does not exceed those obtained at line d_1. The $<V_x'^2>^{0.5}$ profiles at the horizontal plane (not shown) demonstrate the same degree of agreement of the computed data with the experiment.

Note that the experimental dataset [11] contains also the values of the transversal z-velocity $<V_z>$ (in the jet zone they are relatively low, less than 0.05 m/s) and corresponding rms values, $<V_z'^2>^{0.5}$ (of the same order as the $<V_x'^2>^{0.5}$). LES computations reproduce transversal velocity component measurement data with the same quality as the axial velocity.

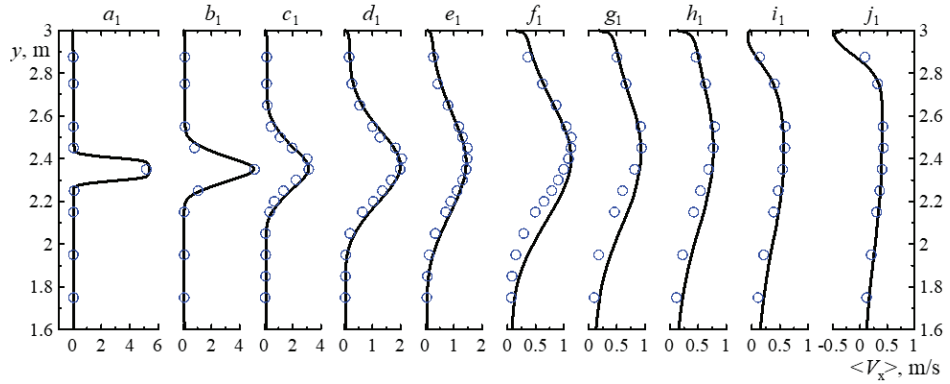

FIGURE 4. Mean longitudinal velocity along vertical lines: CFD results (solid lines) and measurement data [8] (symbols)

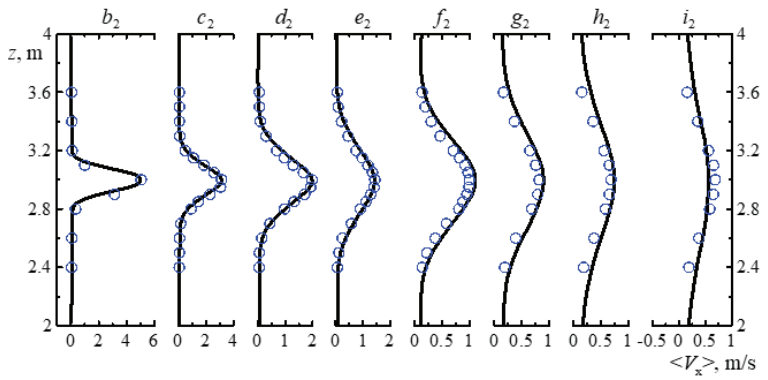

FIGURE 5. Mean longitudinal velocity along horizontal lines: CFD results (solid lines) and measurement data [8] (symbols)

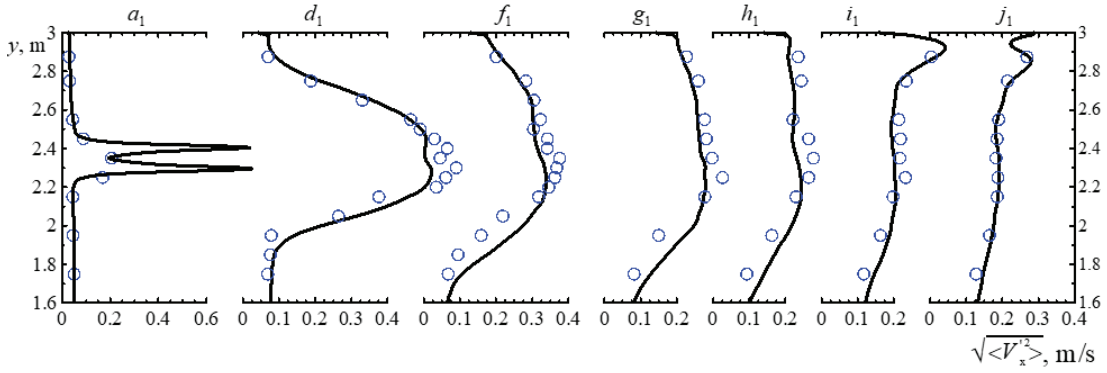

FIGURE 6. Longitudinal rms velocity along vertical lines: CFD results (solid lines) and measurement data [8] (symbols)

Local Velocity Statistics

Figure 7a shows x-velocity evolution in time at three monitoring points placed in the jet zone, points P_1, P_2 and P_3 at various x coordinate values of 1.0, 3.0, 5.0 m; the points are located in the mixing layer at $y = 2.3$ m, $z = 3$ m. The closest to the points are lines c_1, e_1 and h_1 respectively, see Fig. 4 and 6. The plots show data for the sample of 20 seconds corresponding to statistically developed self-oscillating regime. Intensive 3D fluctuations visible in the plots clearly indicate the turbulent behavior of airflow. However, amplitudes and frequencies of the pulsations change much along the jet. From P_1 to P_3 air velocity decreases by the factor of three, the correspondent velocity fluctuations reduction is about four times. Simultaneously, there is a transition to lower frequencies from P_1 to P_3. It is visible also in Fig. 7b where the plots of the power spectral density (PSD) vs. frequency are shown for the same monitoring points. The x-velocity pulsations spectra at points P_1 and P_2 demonstrate a decay range with the power close to the Kolmogorov "-5/3" law corresponding to the inertial region [14]. The energy-containing range at P_1 is up to 5 Hz.

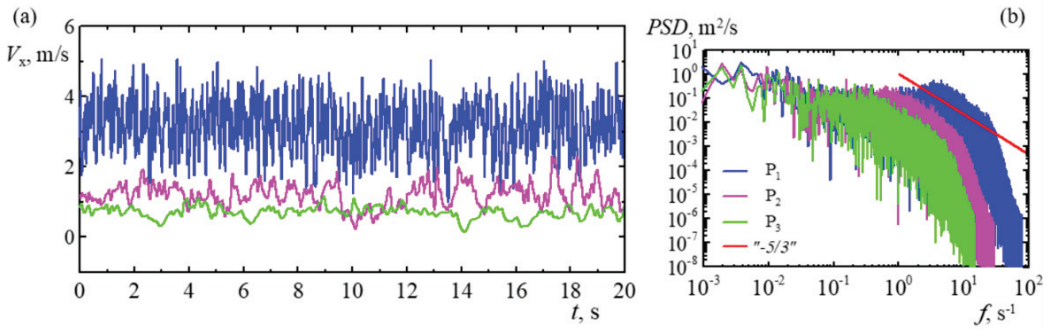

FIGURE 7. (a) Evolution of x-velocity and (b) x-velocity pulsations spectra at monitoring points P_1, P_2 and P_3

Discussion of the accuracy of LES results presented in the previous section is based on the time-averaged velocity component data, as they are directly compared with the LDA results available. Using the time-averaged velocity components, it is possible to calculate the absolute magnitude of the local mean velocity, or simply "velocity", $\mathrm{abs}\langle V\rangle = (\langle V_x\rangle^2+\langle V_y\rangle^2+\langle V_z\rangle^2)^{0.5} \equiv V_m$. However, to assess the thermal comfort and draught risk indexes, it is necessary to operate with the time-averaged value of the local velocity magnitude, or the "speed", $\langle V\rangle \equiv V_a$ [15]. Speed values are directly measured if an omnidirectional hot sphere anemometer is used. CFD solutions based on the RANS approach give the velocity field, but not the speed. To get V_a-distributions required for comfort indexes evaluation from RANS V_m-solutions, it is necessary to use some kind of correction based on semi-empirical correlations. Various correlations aimed at transformation of V_m-data to V_a were suggested in [15-17].

CFD solutions based on the LES approach directly produce data sufficient for statistical evaluation of both the velocity and speed data (as well as the corresponding pulsations), e.g. speed distribution is given in Fig. 3b, while V_m data is illustrated in Fig. 1a. It is evident that the difference between velocity and speed is large in the occupied zone where velocities are relatively low [8]. However, it seems to be useful to discuss this difference for the jet zone being under consideration in the current paper. The discussion is based on the LES dataset with moderate mean velocity value at point P_2 that is located at the distance of 3.0 m from the supply diffuser (purple curves in Fig. 7).

The plots of velocity magnitude and components time evolution at point P_2 during a period of 100 seconds are shown in Fig. 8. Mean and rms velocity values are given in Table 2. As supposed, mean transversal velocity components are close to zero, and the axial velocity (Fig. 8b) makes the main contribution to velocity magnitude. Therefore, the speed value $V_a = 1.30$ m/s (Fig. 8a) is only 6% higher than the mean velocity value $V_m = 1.22$ m/s. The conclusion that the difference between V_m and V_a does not exceed 10% is valid for the entire jet zone with the predominant flow direction. Contrary to substantially different velocity components, their pulsations are comparable: the amplitudes of the transversal pulsations are only 25% less than the longitudinal ones.

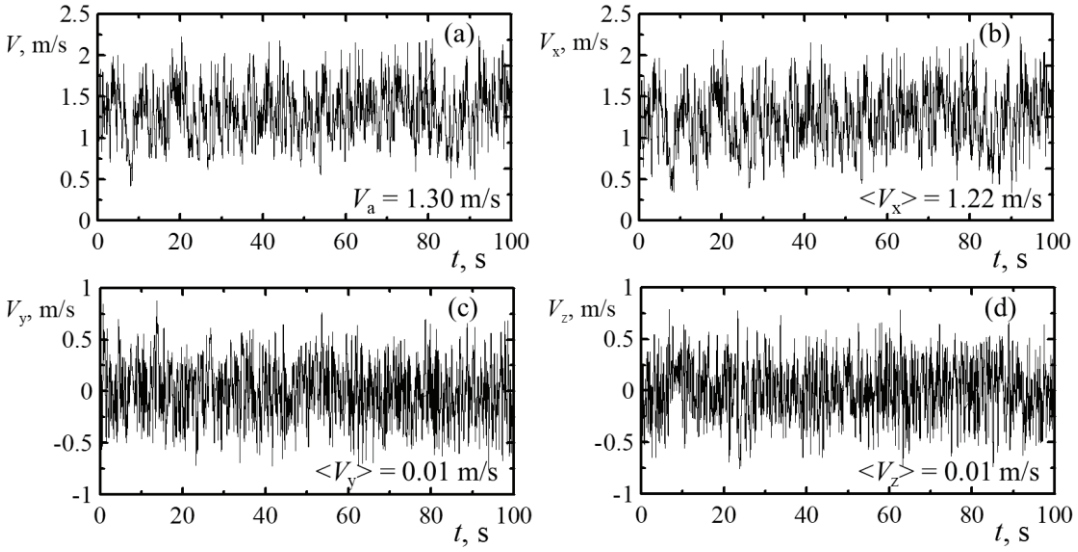

FIGURE 8. Velocity evolution at monitoring point P_2: (a) velocity magnitude and (b) – (d) velocity components

TABLE 2. Statistical evaluation of velocity and speed data at monitoring point P_2

Time-averaged velocity/speed values, m/s				
$\langle V_x\rangle$	$\langle V_y\rangle$	$\langle V_z\rangle$	$V_a = \langle V\rangle$	$V_m = (\langle V_x\rangle^2+\langle V_y\rangle^2+\langle V_z\rangle^2)^{0.5}$
1.22	0.01	0.01	1.30	1.22
Pulsations data				
$\langle V_x'^2\rangle^{0.5}$	$\langle V_y'^2\rangle^{0.5}$	$\langle V_z'^2\rangle^{0.5}$	$\langle V'^2\rangle^{0.5}$	$\{(\langle V_x'^2\rangle+\langle V_y'^2\rangle+\langle V_z'^2\rangle)/3\}^{0.5}$
0.34 m/s	0.26 m/s	0.26 m/s	0.31 m/s	0.29 m/s
$\langle V_x'^2\rangle^{0.5}/V_m$	$\langle V_y'^2\rangle^{0.5}/V_m$	$\langle V_z'^2\rangle^{0.5}/V_m$	Tu_a	Tu_m
0.28	0.21	0.21	0.24	0.24

In general, the amplitudes of both the axial and transversal velocity pulsations are comparable with the mean velocity/speed magnitude. In Table 2, the last row gives the values of turbulence intensity that are defined in different ways for the velocity and speed fields. The speed turbulence intensity is $Tu_a = <V'^2>^{0.5}/V_a = 24\%$ (the last but one column). It is the same as the velocity turbulence intensity, $Tu_m = \{(<V_x'^2>+<V_y'^2>+<V'^2>)/3\}^{0.5}/V_m = 24\%$ (the last column), the difference in the third digit is within the uncertainty of the computed data. Thus, the difference between the speed and velocity turbulence intensity for the point considered is negligible. In general, this conclusion is valid for the central region of the jet zone, outside the initial region and the impingement jet region.

CONCLUSION

Wall-modeled Large Eddy Simulation of indoor airflow in the isothermal ventilated room with a quasi-free sidewall jet at conditions of the benchmark test experiments at Re of 4.57×10^4 have been performed using the ANSYS Fluent 16.2 CFD package. In accordance with the experimental observations, for the ventilation scheme under consideration well-defined division into relatively high-velocity jet zone and the occupied zone with the low-velocity secondary flow was detected. The focus of the study was on the local airflow characteristics in the jet zone only.

Detailed comparison of the LES computational results with the LDA test measurement data on both mean and rms values of the longitudinal and transversal velocity components demonstrated perfect agreement almost everywhere in the jet zone. The only distinction in the axial velocity field was that computations resulted in slight delay of the jet deflection towards the top wall as compared with the experiments. Computations also underestimate to a moderate extent amplitude of pulsations in the jet core.

Both the mean speed and mean velocity data were extracted from the LES solution. The difference between the speed and velocity values does not exceed 10% in the jet zone with the predominant flow direction. The difference between the speed and velocity turbulence intensity is negligible it the central region of the jet zone, outside the initial region and the impingement jet region. The future work will focus on the occupied zone airflow analysis.

REFERENCES

1. R. You, J. Chen, C. H. Lin, D. Wei, H. Sun and Q. Chen, Building and Environment **111**, 110-122 (2017).
2. S. A. Isaev, A. E. Usachov, P. A. Baranov, T. D. Glushkov and M. V. Gureev, J. of Engineering Physics and Thermophysics **90**, 405-411 (2017).
3. A. Palmowska and B. Lipska, Building and Environment **108**, 171-182 (2016).
4. B. Lipska, Z. Trzeciakiewicz, J. Ferdyn-Grygierek, Z. Popiolek, Indoor Built Environ. **21**, 332-337 (2012).
5. C. H. Son, E. H. Turner, N. G. Ivanov, D. S. Telnov and E. M. Smirnov, "Integrated Computational Fluid Dynamics carbon dioxide concentration study for the International Space Station," in *Proc. of the 35th Int. Conf. on Environmental Systems*, SAE Technical Paper 2005-01-2795 (SAE International, 2005), pp. 1-6.
6. C. H. Son, N. G. Ivanov, D. S. Telnov and E. M. Smirnov, "Numerical Study of Ammonia Leak and Dispersion in the International Space Station," in *Proc. of the 42nd Int. Conf. on Environmental Systems* (American Institute for Aeronautics and Astronautics, 2012), pp. 1-10.
7. U. Piomelli, Phil. Trans. R. Soc. A **372**, 1-13 (2014).
8. M. Hurnik, M. Blaszczok and Z. Popiolek, Building and Environment **93**, 319-330 (2015).
9. P. V. Nielsen, A. Restivo and J. H. Whitelaw, ASME J. Fluids Engineering **100**, 291-298 (1978).
10. J. D. Posner, C. R. Buchanan, D. Dunn-Rankin, Energy and Buildings **35**, 515-526 (2003).
11. M. Hurnik and Z. Popiolek, Data in Brief **5**, 213-217 (2015).
12. N. G. Ivanov and M. A. Zasimova, "Large Eddy Simulation of airflow in a test ventilated room," in *Int. Conf. PhysicA.SPb/2017* (IOP Publishing, accepted for publication), pp. 1-6.
13. M. L. Shur, P. R. Spalart, M. K. Strelets and A. K. Travin, Int. J. Heat and Fluid Flow **29** (6), 1638-1649 (2008).
14. J. O. Hinze, *Turbulence* (New York: McGraw-Hill, 1975).
15. H. Koskela, J. Heikkinen, R. Niemela and T. Hautalampi, Building and Environment **36** (2), 247-255 (2001).
16. E. M. Smirnov, N. G. Ivanov, D. S. Telnov, C. H. Son and V. K. Aksamentov, "Computational Fluid Dynamics Study of Air Flow Characteristics in the Columbus Module," in *Proc. of the 34th Int. Conf. on Environmental Systems*, SAE Technical Paper 2004-01-2500 (SAE International, 2004), pp. 1-8.
17. Z. Popiolek and A. Melikov, "Improvement of CFD predictions of air speed turbulence intensity and draught discomfort," in *Indoor Air 2008: 11 Int. Conf. on Indoor Air Quality and Climate* (Copenhagen, 2008), pp. 1-8.